Modeling Steel Frame Buildings in Three Dimensions - Part II: Elastofiber Beam Element and Examples

Swaminathan Krishnan [1] and John F. Hall [2]

Keywords: Steel Frames, Nonlinear Analysis, Panel Zone, Elastofiber.

ABSTRACT

This is the second of two papers describing a procedure for the three dimensional nonlinear time-history analysis of steel framed buildings. An overview of the procedure and the theory for the panel zone element and the plastic hinge beam element are presented in Part I. In this paper, the theory for an efficient new element for modeling beams and columns in steel frames called the elastofiber element is presented, along with four illustrative examples. The elastofiber beam element is divided into three segments - two end nonlinear segments and an interior elastic segment. The cross-sections of the end segments are subdivided into fibers. Associated with each fiber is a nonlinear hysteretic stress-strain law for axial stress and strain. This accounts for coupling of nonlinear material behavior between bending about the major and minor axes of the cross-section and axial deformation. Examples presented include large deflection of an elastic cantilever, cyclic loading of a cantilever beam, pushover analysis of a 20-story steel moment-frame building to collapse, and strong ground motion analysis of a 2-story unsymmetric steel moment-frame building.

[1]Post-Doctoral Scholar, Seismological Laboratory, MC 252-21, California Institute of Technology, Pasadena, CA-91125. Email: krishnan@caltech.edu

[2]Professor, Civil Engineering and Applied Mechanics, MC 104-44, California Institute of Technology, Pasadena, CA-91125

INTRODUCTION

Beams and columns in buildings have been modeled using fiber elements (Hall and Challa 1995; Kaba and Mahin 1984; Mark 1976) in order to more accurately account for nonlinear material behavior under combined bending and axial load, such as strength interaction, strain hardening, cracking, and spread of nonlinearity along the member. A fiber element is subdivided into a number of segments along its length and each segment is further subdivided into a number of fibers in the cross-section. Associated with each fiber is a nonlinear hysteretic relation for axial stress-strain. Because of the extra degrees of freedom (DOF) due to the segmentation and the large number of hysteretic relations to follow (one for each fiber, 200 or more fibers for a single 3-dimensional element), the computational requirements can become considerable, especially for large structures which, because of some features such as irregularity, must be modeled in three dimensions.

To reduce these heavy computational requirements of the fully discretized fiber element, a new hybrid element called the elastofiber element is introduced here. The elastofiber element is divided into three segments - two end nonlinear ones and an interior elastic one. The end segments are fiber segments while the interior segment is modeled as a plastic hinge element as discussed in the companion paper except that it remains elastic, i.e., no axial yielding or plastic hinging.

THREE-DIMENSIONAL ELASTOFIBER BEAM ELEMENT

General Description

The elastofiber element can model beams and columns in framed structures. Assumptions listed in the companion paper for the plastic hinge element are maintained: uniform cross-section along the length, doubly symmetric cross-section, plane sections remain plane, small strains, small lateral deflections relative to the chord, no warping restraint, and no along-span loads.

The elastofiber beam element has 3 segments and 4 nodes (Figure 1). Two nodes numbered 1 and 2 are located at the ends and connect to the attachment points a through f of the panel zone

element. As in the case of the plastic hinge element, columns connect to attachment points e and f while beams connect to attachment points a through d. The other two nodes are interior and are numbered 3 and 4. Original length of a segment is denoted by L_{s0}. Segment 1 goes from node 1 to node 3, segment 2 from node 3 to node 4, and segment 3 from node 4 to node 2.

Each segment has its own local coordinate system, $X'Y'Z'$, which is right-handed and orthogonal. Axes are defined in the same manner as for the plastic hinge element. X' runs along the longitudinal axis of each segment at the centroid of the cross-section oriented from node 1 to node 3 for segment 1, from node 3 to node 4 for segment 2, and from node 4 to node 2 for segment 3. All the nodes are located at the centroid of the cross-section. Y' and Z' are major and minor principal axes of the cross-section of each segment, respectively. They are oriented in the same way as for the plastic hinge element using the orientation angle, α_{or}. Each $X'Y'Z'$ system translates and rotates with its associated segment. Initially, a beam element is straight and each of the three $X'Y'Z'$ systems has the same orientation.

The middle segment of the elastofiber beam element is an elastic version of the plastic hinge beam element, i.e., no axial yielding and no plastic hinging. End segments are fiber segments. As shown in Figure 1, fiber segment cross-sections are divided into 20 fibers; each fiber runs the length of the segment. Associated with each fiber is a nonlinear hysteretic stress-strain law for axial stress, σ_n, and axial strain, ϵ_n, where n denotes the n^{th} fiber. The fiber segment is based on finite element methodology wherein the beam translations and rotations are interpolated linearly and independently from their nodal values. This requires a one-point integration on the shear terms to prevent locking.

Because of the presence of the interior nodes, the updating process for each elastofiber beam element requires a nonlinear structural analysis. Iterations for each element are performed within each global iteration. These multi-segment element analyses are carried out with degrees of freedom transformed to the global coordinate system XYZ. This extra step is necessary because the degrees of freedom at the two interior nodes 3 and 4 are not included as global degrees of freedom.

Similar to the case of a plastic hinge element, the capabilities of an elastofiber element can be enhanced by the use of additional interior nodes. These capabilities include the application of gravity loads along the member, the effects of bowing, and post-buckling of a brace. Since brace post-buckling can involve flexural yielding at some point along the length, an additional fiber segment is necessary there. Locating a short fiber segment at mid-length would probably suffice for many applications. This feature is not implemented here.

Degrees of Freedom of a Segment, and Nodal Forces and Moments

The degrees of freedom of a segment of the elastofiber element are shown in Figure 2, where the nodal pairs (1,3), (3,4) and (4,2) are denoted by (i, j):

1. U_i, U_j = X' translations of nodes i and j, respectively.
2. $V_{iY'}$, $V_{jY'}$ = Y' translations of nodes i and j, respectively.
3. $V_{iZ'}$, $V_{jZ'}$ = Z' translations of nodes i and j, respectively.
4. α_i, α_j = rotations about X' at nodes i and j, respectively.
5. $\theta_{iY'}$, $\theta_{jY'}$ = rotations about Y' at nodes i and j, respectively.
6. $\theta_{iZ'}$, $\theta_{jZ'}$ = rotations about Z' at nodes i and j, respectively.

Corresponding to these degrees of freedom are nodal forces and moments (Figure 2):

1. P_i, P_j = forces in X' direction at nodes i and j, respectively.
2. $Q_{iY'}$, $Q_{jY'}$ = forces in Y' direction at nodes i and j, respectively.
3. $Q_{iZ'}$, $Q_{jZ'}$ = forces in Z' direction at nodes i and j, respectively.
4. T_i, T_j = moments about X' axis at nodes i and j, respectively.

5. $M_{iY'}$, $M_{jY'}$ = moments about Y' axis at nodes i and j, respectively.

6. $M_{iZ'}$, $M_{jZ'}$ = moments about Z' axis at nodes i and j, respectively.

Internal Forces and Moments in a Segment

The internal forces and moments in a segment of the elastofiber beam element are the axial force, P, the shear forces in the Y' and Z' directions, $Q_{Y'}$ and $Q_{Z'}$, respectively, the twisting moment (torque), T, and the bending moments about the Y' and Z' axes, $M_{Y'}$ and $M_{Z'}$, respectively. The sign convention (positive directions) for these forces and moments is the same as that for the plastic hinge element (Figure 8 in the companion paper).

Transformation Matrix $[T_{ef}]$

$[T_{ef}]$ is the transformation matrix between the 16 global DOF at the nodes J and K of the joints, $\{\Delta U_{ef}\}$, and the 12 degrees of freedom at nodes 1 and 2 of the elastofiber element, $\{\Delta U_{ef}\}_L$. Because the element computations are done for DOF transformed to the XYZ coordinate system, the terms in $\{\Delta U_{ef}\}_L$ are with respect to XYZ. Thus, only the first three transformation steps, discussed in the companion paper for the plastic hinge beam element, are necessary. The incremental displacement vectors, $\{\Delta U_{ph}\}_L$, $\{\Delta \bar{U}_{ph}\}_L$, $\{\Delta \bar{U}_{ph}\}$, and $\{\Delta U_{ph}\}$ mentioned there contain the same terms as the elastofiber element, and are renamed $\{\Delta U_{ef}\}_L$, $\{\Delta \bar{U}_{ef}\}_L$, $\{\Delta \bar{U}_{ef}\}$, and $\{\Delta U_{ef}\}$ respectively. The transformation matrix is

$$[T_{ef}] = [T_3]\,[T_2]\,[T_1]\,. \tag{1}$$

Material Model for Fiber Axial Stress-Strain

The hysteresis model for axial stress-strain behavior of a fiber proposed by (Hall and Challa 1995) defines a backbone curve as shown in Figure 3. It consists of a linear portion, a yield plateau,

a strain-hardening region which is described by a cubic ellipse, and a strain softening region described by a continuation of the same cubic ellipse. The backbone curve is characterized by seven parameters: yield stress σ_y, ultimate stress σ_u, Young's modulus E, strain at initiation of strain hardening ϵ_{sh}, strain at ultimate stress ϵ_u, rupture strain ϵ_r, and the tangent modulus at initiation of strain hardening E_{sh}. Hysteresis loops (Figure 3) consist of linear segments and cubic ellipses, and the hysteretic rules to define the cyclic response of each panel are given by (Challa 1992). Although not included here, a fiber fracture capability can be added to approximately represent fracture of welded beam-to-column connections (Hall 1995).

Development of the Tangent Stiffness Matrix for a Fiber Segment

Because of the linear interpolation, the axial strain ϵ_n in fiber n is constant along the length of the segment. A strain increment $d\epsilon_n$ is caused by nodal displacement increments as follows:

$$d\epsilon_n = \frac{dU_j - dU_i}{L_{s0}} + \frac{Z'_n\,(d\phi_{jY'} - d\phi_{iY'})}{L_{s0}} - \frac{Y'_n\,(d\phi_{jZ'} - d\phi_{iZ'})}{L_{s0}} \tag{2}$$

where the rotations of the cross-section $\phi_{iY'}$, $\phi_{jY'}$, $\phi_{iZ'}$, and $\phi_{jZ'}$ about Y' and Z' at the nodes are relative to the chord (straight line connecting nodes i and j of the segment), and Y'_n and Z'_n are the Y' and Z' coordinates of fiber n. Figure 1 shows the actual fiber layouts for I sections and box sections. The axial stress σ_n is related to the axial strain ϵ_n by the incremental relation

$$d\sigma_n = E_{T,n} d\epsilon_n \tag{3}$$

where $E_{T,n}$ is the tangent modulus of the fiber determined from the fiber material model. The internal axial force P and bending moments $M_{Y'}$ and $M_{Z'}$ are expressed by summing over the fibers as follows.

$$P = \sum_n \sigma_n A_n \tag{4}$$

$$\bar{M}_{Y'} = -\sum_n \sigma_n A_n Z'_n \tag{5a}$$

$$\bar{M}_{Z'} = \sum_n \sigma_n A_n Y'_n \tag{5b}$$

where A_n is the cross-sectional area of fiber n. These two moment expressions will only be used for the moments at mid-length of the segment, and this is denoted by $\bar{}$.

Expressions for the internal shear forces are expressed using elastic theory and properties of the entire cross-section:

$$Q_{Y'} = -A_{SY'} G \phi_{Z'} \tag{6a}$$

$$Q_{Z'} = A_{SZ'} G \phi_{Y'} \tag{6b}$$

where $A_{SY'}$ and $A_{SZ'}$ are the effective shear areas of the cross-section in the Y' and Z' directions (Figure 15 in the companion paper), $\phi_{Y'}$ and $\phi_{Z'}$ are the rotations of the cross-section about Y' and Z' along the beam relative to the chord, and G is the shear modulus. The shear forces will be assumed constant along the beam at their values at mid-length to prevent shear locking. Using the $\bar{}$ notation,

$$\bar{Q}_{Y'} = -A_{SY'} G \frac{\phi_{iZ'} + \phi_{jZ'}}{2} \tag{7a}$$

$$\bar{Q}_{Z'} = A_{SZ'} G \frac{\phi_{iY'} + \phi_{jY'}}{2}. \tag{7b}$$

Incremental versions of eqns. 4, 5, and 7, are as follows:

$$dP = \sum_n E_{T,n} A_n d\epsilon_n \tag{8}$$

$$d\bar{M}_{Y'} = -\sum_n E_{T,n} A_n Z'_n d\epsilon_n \tag{9a}$$

$$d\bar{M}_{Z'} = \sum_n E_{T,n} A_n Y'_n d\epsilon_n \tag{9b}$$

using eqn. 3 and

$$d\bar{Q}_{Y'} = -A_{SY'} G \frac{d\phi_{iZ'} + d\phi_{jZ'}}{2} \tag{10a}$$

$$d\bar{Q}_{Z'} = A_{SZ'} G \frac{d\phi_{iY'} + d\phi_{jY'}}{2}. \tag{10b}$$

For twisting, similar to the plastic hinge element,

$$dT = GJ d\omega \tag{11a}$$

$$d\omega = \frac{d\alpha_j - d\alpha_i}{L_{s0}} \tag{11b}$$

$$dT = GJ \frac{d\alpha_j - d\alpha_i}{L_{s0}}. \tag{11c}$$

Substituting eqn. 2 into eqns. 8 through 11, the incremental relations can be written in matrix form as

$$\begin{Bmatrix} dP \\ d\bar{M}_{Y'} \\ d\bar{M}_{Z'} \\ d\bar{Q}_{Y'} \\ d\bar{Q}_{Z'} \\ dT \end{Bmatrix} = [C_T] \begin{Bmatrix} \frac{dU_j - dU_i}{L_{s0}} \\ -\frac{\left(d\phi_{jY'} - d\phi_{iY'}\right)}{L_{s0}} \\ -\frac{\left(d\phi_{jZ'} - d\phi_{iZ'}\right)}{L_{s0}} \\ -\frac{d\phi_{iZ'} + d\phi_{jZ'}}{2} \\ \frac{d\phi_{iY'} + d\phi_{jY'}}{2} \\ \frac{d\alpha_j - d\alpha_i}{L_{s0}} \end{Bmatrix} \tag{12}$$

where

$$[C_T] = \begin{bmatrix} \sum_n E_{T,n}A_n & -\sum_n E_{T,n}A_nZ'_n & \sum_n E_{T,n}A_nY'_n & 0 & 0 & 0 \\ & \sum_n E_{T,n}A_nZ'^2_n & -\sum_n E_{T,n}A_nY'_nZ'_n & 0 & 0 & 0 \\ & & \sum_n E_{T,n}A_nY'^2_n & 0 & 0 & 0 \\ & symmetric & & A_{SY'}G & 0 & 0 \\ & & & & A_{SZ'}G & 0 \\ & & & & & GJ \end{bmatrix}. \quad (13)$$

The right hand side vector of eqn. 12 is expressed in terms of nodal degrees of freedom as

$$\begin{Bmatrix} \frac{dU_j - dU_i}{L_{s0}} \\ -\frac{\left(d\phi_{jY'} - d\phi_{iY'}\right)}{L_{s0}} \\ -\frac{\left(d\phi_{jZ'} - d\phi_{iZ'}\right)}{L_{s0}} \\ -\frac{d\phi_{iZ'} + d\phi_{jZ'}}{2} \\ \frac{d\phi_{iY'} + d\phi_{jY'}}{2} \\ \frac{d\alpha_j - d\alpha_i}{L_{s0}} \end{Bmatrix} = \frac{1}{L_{s0}}[S] \begin{Bmatrix} dU_i \\ dV_{iY'} \\ dV_{iZ'} \\ d\alpha_i \\ d\theta_{iY'} \\ d\theta_{iZ'} \\ dU_j \\ dV_{jY'} \\ dV_{jZ'} \\ d\alpha_j \\ d\theta_{jY'} \\ d\theta_{jZ'} \end{Bmatrix} \quad (14)$$

where

$$[S] = \begin{bmatrix} -1 & 0 & 0 & 0 & 0 & 0 & 1 & 0 & 0 & 0 & 0 & 0 \\ 0 & 0 & 0 & 0 & 1 & 0 & 0 & 0 & 0 & 0 & -1 & 0 \\ 0 & 0 & 0 & 0 & 0 & 1 & 0 & 0 & 0 & 0 & 0 & -1 \\ 0 & -1 & 0 & 0 & 0 & -\frac{L_{s0}}{2} & 0 & 1 & 0 & 0 & 0 & -\frac{L_{s0}}{2} \\ 0 & 0 & -1 & 0 & \frac{L_{s0}}{2} & 0 & 0 & 0 & 1 & 0 & \frac{L_{s0}}{2} & 0 \\ 0 & 0 & 0 & -1 & 0 & 0 & 0 & 0 & 0 & 1 & 0 & 0 \end{bmatrix}. \tag{15}$$

In incremental form, the nodal forces and moments are expressed in terms of the internal ones as

$$\begin{Bmatrix} dP_i \\ dQ_{iY'} \\ dQ_{iZ'} \\ dT_i \\ dM_{iY'} \\ dM_{iZ'} \\ dP_j \\ dQ_{jY'} \\ dQ_{jZ'} \\ dT_j \\ dM_{jY'} \\ dM_{jZ'} \end{Bmatrix} = [S]^T \begin{Bmatrix} dP \\ d\bar{M}_{Y'} \\ d\bar{M}_{Z'} \\ d\bar{Q}_{Y'} \\ d\bar{Q}_{Z'} \\ dT \end{Bmatrix} + \frac{P}{L_{s0}} \begin{bmatrix} 0 & 0 & 0 & 0 & 0 & 0 & 0 & 0 & 0 & 0 & 0 & 0 \\ 0 & 1 & 0 & 0 & 0 & 0 & 0 & -1 & 0 & 0 & 0 & 0 \\ 0 & 0 & 1 & 0 & 0 & 0 & 0 & 0 & -1 & 0 & 0 & 0 \\ 0 & 0 & 0 & 0 & 0 & 0 & 0 & 0 & 0 & 0 & 0 & 0 \\ 0 & 0 & 0 & 0 & 0 & 0 & 0 & 0 & 0 & 0 & 0 & 0 \\ 0 & 0 & 0 & 0 & 0 & 0 & 0 & 0 & 0 & 0 & 0 & 0 \\ 0 & 0 & 0 & 0 & 0 & 0 & 0 & 0 & 0 & 0 & 0 & 0 \\ 0 & -1 & 0 & 0 & 0 & 0 & 0 & 1 & 0 & 0 & 0 & 0 \\ 0 & 0 & -1 & 0 & 0 & 0 & 0 & 0 & 1 & 0 & 0 & 0 \\ 0 & 0 & 0 & 0 & 0 & 0 & 0 & 0 & 0 & 0 & 0 & 0 \\ 0 & 0 & 0 & 0 & 0 & 0 & 0 & 0 & 0 & 0 & 0 & 0 \\ 0 & 0 & 0 & 0 & 0 & 0 & 0 & 0 & 0 & 0 & 0 & 0 \end{bmatrix} \begin{Bmatrix} dU_i \\ dV_{iY'} \\ dV_{iZ'} \\ d\alpha_i \\ d\theta_{iY'} \\ d\theta_{iZ'} \\ dU_j \\ dV_{jY'} \\ dV_{jZ'} \\ d\alpha_j \\ d\theta_{jY'} \\ d\theta_{jZ'} \end{Bmatrix} \tag{16}$$

where the matrix consisting of $\frac{P}{L_{s0}}$ terms is the geometric stiffness matrix, $[G]$. Combining the above leads to

$$\{dR'_s\} = \left[K'_{T,s}\right] \{dU'_s\} \tag{17}$$

where $\{dR'_s\}$ is the incremental version of

$$\langle R'_s \rangle = \langle \; P_i \quad Q_{iY'} \quad Q_{iZ'} \quad T_i \quad M_{iY'} \quad M_{iZ'} \quad P_j \quad Q_{jY'} \quad Q_{jZ'} \quad T_j \quad M_{jY'} \quad M_{jZ'} \; \rangle, \tag{18}$$

$\left[K'_{T,s}\right]$ is the 12×12 tangent stiffness matrix for a fiber segment:

$$\left[K'_{T,s}\right] = \frac{1}{L_{s0}} \left[S\right]^T \left[C_T\right] \left[S\right] + \left[G\right], \tag{19}$$

and

$$\langle dU'_s \rangle = \langle \; dU_i \quad dV_{iY'} \quad dV_{iZ'} \quad d\alpha_i \quad d\theta_{iY'} \quad d\theta_{iZ'} \quad dU_j \quad dV_{jY'} \quad dV_{jZ'} \quad d\alpha_j \quad d\theta_{jY'} \quad d\theta_{jZ'} \; \rangle. \tag{20}$$

Updating Process

In global iteration l, $\{\Delta U\}$ is computed from eqn. 7 in the companion paper. The 12 displacement increments in the XYZ coordinate system at nodes 1 and 2 for an elastofiber element are found as

$$\left\{\Delta U_{ef}\right\}_L = \left[T^l_{ef}\right] \left\{\Delta U_{ef}\right\} \tag{21}$$

where $\{\Delta U_{ef}\}$ contains the 16 terms extracted from $\{\Delta U\}$ corresponding to the nodes J and K connected to element nodes 1 and 2, and $\left[T^l_{ef}\right]$ is the transformation matrix representing configuration l.

Updating the panel zone element geometries leads to $\left[T_1^{l+1}\right]$, $\left[T_2^{l+1}\right]$, and $\left[T_3^{l+1}\right]$ as discussed in the companion paper. Then the updated transformation matrix is computed as

$$\left[T^{l+1}_{ef}\right] = \left[T_3^{l+1}\right] \left[T_2^{l+1}\right] \left[T_1^{l+1}\right]. \tag{22}$$

Next, the displacement increments $\left\{\Delta U_{ef}\right\}_L$ are applied to nodes 1 and 2 of the elastofiber element, and the resulting displacements of nodes 3 and 4 computed by an iterative structural analysis. In the k^{th} iteration of this process (iteration (k) where the $()$ denotes element iterations

within global iteration l), the equation to be solved is

$$\begin{bmatrix} K_{T,II}^{(k)} & K_{T,IE}^{(k)} \\ K_{T,EI}^{(k)} & K_{T,EE}^{(k)} \end{bmatrix} \begin{Bmatrix} \Delta U_I \\ \Delta U_E \end{Bmatrix} = \begin{Bmatrix} 0 \\ F_E \end{Bmatrix} - \begin{Bmatrix} R_I^{(k)} \\ R_E^{(k)} \end{Bmatrix} \tag{23}$$

which has been partitioned into the 12 DOF group I at the interior nodes 3 and 4, and the 12 DOF group E at the end nodes 1 and 2, where

$$\begin{bmatrix} K_{T,II}^{(k)} & K_{T,IE}^{(k)} \\ K_{T,EI}^{(k)} & K_{T,EE}^{(k)} \end{bmatrix} \text{ and } \begin{Bmatrix} R_I^{(k)} \\ R_E^{(k)} \end{Bmatrix}$$

are the tangent stiffness matrix and stiffness force vector for configuration (k) respectively; $\{F_E\}$ is a vector of unknown loads applied to the element through nodes 1 and 2 by the surrounding structure; and $\{\Delta U_E\}$ is set to $\{\Delta U_{ef}\}_L$ for iteration $(k) = 1$ and to 0 for iteration $(k) > 1$. Eqn. 23 is solved for $\{\Delta U_I\}$ by substituting in the known vector $\{\Delta U_E\}$ and then solving the upper partitioned equation, which does not involve $\{F_E\}$. Iterations continue to convergence to the global $l + 1$ state at which point the tangent stiffness matrix and stiffness force vector are denoted by

$$\begin{bmatrix} K_{T,II}^{l+1} & K_{T,IE}^{l+1} \\ K_{T,EI}^{l+1} & K_{T,EE}^{l+1} \end{bmatrix} \text{ and } \begin{Bmatrix} R_I^{l+1} \\ R_E^{l+1} \end{Bmatrix}.$$

These are used to start the elastofiber element analysis at $(k) = 1$ after global iteration $l + 1$.

The contributions to the global $\left[K_T^{l+1}\right]$ and $\left\{R^{l+1}\right\}$ (see discussion following eqn. 7 in the companion paper) are obtained from the $l+1$ tangent stiffness matrix and stiffness force vector by condensing out the I degrees of freedom:

$$\left[K_{T,ef}^{l+1}\right]_L = \left[K_{T,EE}^{l+1}\right] - \left[K_{T,EI}^{l+1}\right]\left[K_{T,II}^{l+1}\right]^{-1}\left[K_{T,IE}^{l+1}\right] \tag{24}$$

$$\left\{R_{ef}^{l+1}\right\}_L = \left\{R_E^{l+1}\right\} - \left[K_{T,EI}^{l+1}\right]\left[K_{T,II}^{l+1}\right]^{-1}\left\{R_I^{l+1}\right\} \tag{25}$$

and then transformation to

$$\left[K_{T,ef}^{l+1}\right] = \left[T_{ef}^{l+1}\right]^T \left[K_{T,ef}^{l+1}\right]_L \left[T_{ef}^{l+1}\right] \tag{26a}$$

$$\left\{R_{ef}^{l+1}\right\} = \left[T_{ef}^{l+1}\right]^T \left\{R_{ef}^{l+1}\right\}_L . \tag{26b}$$

These are assembled into $\left[K_T^{l+1}\right]$ and $\left\{R^{l+1}\right\}$.

The element matrix $\begin{bmatrix} K_{T,II} & K_{T,IE} \\ K_{T,EI} & K_{T,EE} \end{bmatrix}$ and vector $\begin{Bmatrix} R_I \\ R_E \end{Bmatrix}$ are assembled from the segment quantities $\left[K'_{T,s}\right]$ and $\{R'_s\}$ defined in eqns. 19 and 18 after transformation to XYZ by

$$[K_{T,s}] = [T_s]^T \left[K'_{T,s}\right] [T_s] \tag{27}$$

$$\{R_s\} = [T_s]^T \{R'_s\} \tag{28}$$

where $[T_s]$ is the same as $[T_4]$ given by eqn. 34 in the companion paper, but based on the segment $X'Y'Z'$.

The updating process for $[T_s]$, $\{R'_s\}$, and $\left[K'_{T,s}\right]$ during the element iterations is described now. The $\{\Delta U_I\}$ computed from eqn. 23 in iteration (k) along with the initial $\{\Delta U_E\}$ are used to update the locations of the four element nodes. This leads to a new direction for the X' axis of each segment. Then terms from $\{\Delta U_E\}$ and $\{\Delta U_I\}$ are extracted and stored in $\{\Delta U_s\}$ for each segment, and then transformed to the $X'Y'Z'$ coordinate system by

$$\{\Delta U'_s\} = \left[T_s^{(k)}\right] \{\Delta U_s\} . \tag{29}$$

Using $\Delta\alpha_i$ and $\Delta\alpha_j$ from $\{\Delta U'_s\}$, α_{or} is updated, and then $\left[T_s^{(k+1)}\right]$ is found as discussed in the companion paper for $\left[T_4^{l+1}\right]$ of the plastic hinge element.

For the middle segment, $\left\{R_s'^{(k+1)}\right\}$ and $\left[K_{T,s}'^{(k+1)}\right]$ are found by the procedure used for the plastic hinge element except that no plastic hinges are allowed to form.

For a fiber segment, first consider $\left\{R_s^{\prime(k+1)}\right\}$. The $\Delta\phi$ rotation increments are computed as

$$\Delta\phi_{iY'} = \Delta\theta_{iY'} + \frac{\Delta V_{jZ'} - \Delta V_{iZ'}}{L_{s0}} \tag{30a}$$

$$\Delta\phi_{jY'} = \Delta\theta_{jY'} + \frac{\Delta V_{jZ'} - \Delta V_{iZ'}}{L_{s0}} \tag{30b}$$

$$\Delta\phi_{iZ'} = \Delta\theta_{iZ'} - \frac{\Delta V_{jY'} - \Delta V_{iY'}}{L_{s0}} \tag{30c}$$

$$\Delta\phi_{jZ'} = \Delta\theta_{jZ'} - \frac{\Delta V_{jY'} - \Delta V_{iY'}}{L_{s0}} \tag{30d}$$

where the right-side terms are from $\{\Delta U_s'\}$. Along with ΔU_i and ΔU_j, also from $\{\Delta U_s'\}$, $\Delta\epsilon_n$ is found for each fiber from eqn. 2. Then, using the fiber material model, the updated stresses $\sigma_n^{(k+1)}$ are found, and from eqns. 4 and 5:

$$P^{(k+1)} = \sum_n \sigma_n^{(k+1)} A_n \tag{31}$$

$$\bar{M}_{Y'}^{(k+1)} = -\sum_n \sigma_n^{(k+1)} A_n Z_n' \tag{32a}$$

$$\bar{M}_{Z'}^{(k+1)} = \sum_n \sigma_n^{(k+1)} A_n Y_n'. \tag{32b}$$

The internal shear forces are updated as

$$\bar{Q}_{Y'}^{(k+1)} = \bar{Q}_{Y'}^{(k)} - A_{SY'} G \frac{\Delta\phi_{iZ'} + \Delta\phi_{jZ'}}{2} \tag{33a}$$

$$\bar{Q}_{Z'}^{(k+1)} = \bar{Q}_{Z'}^{(k)} + A_{SZ'} G \frac{\Delta\phi_{iY'} + \Delta\phi_{jY'}}{2} \tag{33b}$$

and the internal twisting moment is updated as

$$T^{(k+1)} = T^{(k)} + GJ \frac{\Delta\alpha_j - \Delta\alpha_i}{L_{s0}}. \tag{34}$$

The nodal forces and moments can now be computed using the $[S]$ matrix as in the left part of eqn. 16:

$$P_j^{(k+1)} = -P_i^{(k+1)} = P^{(k+1)} \tag{35a}$$

$$Q_{jY'}^{(k+1)} = -Q_{iY'}^{(k+1)} = \bar{Q}_{Y'}^{(k+1)} \tag{35b}$$

$$Q_{jZ'}^{(k+1)} = -Q_{iZ'}^{(k+1)} = \bar{Q}_{Z'}^{(k+1)} \tag{35c}$$

$$T_j^{(k+1)} = -T_i^{(k+1)} = T^{(k+1)} \tag{35d}$$

$$M_{iY'}^{(k+1)} = \bar{M}_{Y'}^{(k+1)} + \bar{Q}_{Z'}^{(k+1)} \frac{L_{s0}}{2} \tag{35e}$$

$$M_{iZ'}^{(k+1)} = \bar{M}_{Z'}^{(k+1)} - \bar{Q}_{Y'}^{(k+1)} \frac{L_{s0}}{2} \tag{35f}$$

$$M_{jY'}^{(k+1)} = -\bar{M}_{Y'}^{(k+1)} + \bar{Q}_{Z'}^{(k+1)} \frac{L_{s0}}{2} \tag{35g}$$

$$M_{jZ'}^{(k+1)} = -\bar{M}_{Z'}^{(k+1)} - \bar{Q}_{Y'}^{(k+1)} \frac{L_{s0}}{2}. \tag{35h}$$

These are assembled into $\left\{ R_s'^{(k+1)} \right\}$.

After $\left\{ R_s'^{(k+1)} \right\}$ is computed for a fiber segment, $P^{(k+1)}$ for the segment and $E_{T,n}^{(k+1)}$ for each fiber will be known. Then, $\left[K_{T,s}'^{(k+1)} \right]$ can be computed using the formulae of the previous section.

Calibration of Fiber Segment Length

The length of the fiber segment in relation to the total length of the elastofiber element has to be calibrated to give best results. This calibration is carried out on a single element model of a simply supported $W30 \times 116$ beam (Figure 4) that is 6.096 m (20 $feet$) long. A572-Grade 50 steel with $\sigma_y = 345\ MPa\ (50\ ksi)$ and $\sigma_u = 448\ MPa\ (65\ ksi)$ is used. Other parameters are $E = 2 \times 10^5\ MPa\ (29000\ ksi)$, $\epsilon_{sh} = 0.012$, $\epsilon_u = 0.160$, $\epsilon_r = 0.308$, $E_{sh} = 4000\ MPa\ (580\ ksi)$, and $G = 8 \times 10^4\ MPa\ (11600\ ksi)$. The elastofiber element is calibrated against a 2-dimensional, 8-segment fiber element (Hall and Challa 1995) which should be more accurate because of the greater number of segments. The beam is subjected to the rotation history shown in Figure 4 at

both ends. These rotations force the beam into double curvature similar to the situation of a beam or column that is part of a frame subjected to lateral loading. No axial restraint is imposed.

Results using a fiber segment length of 3% of the length of the elastofiber element are presented in Figure 5. These include histories of the moment M generated at the ends of the beam, and the moment plotted against the rotation θ at the ends. The elastofiber element performance compares well to that of the more accurate 8-segment fiber element although some differences are evident over one cycle of response in the middle of the history. This difference is attributed to the rupture of some flange fibers which takes place at different times for the two elements (a half cycle apart). Overall, this is a relatively minor deviation which does not occur until a very large plastic rotation is reached.

Similar plots appear in Figure 6 for A36 steel with $\sigma_y = 248\ MPa\ (36\ ksi)$ and $\sigma_u = 400\ MPa\ (58\ ksi)$. Other parameters are taken to be the same as those in the previous case. Good agreement is achieved by increasing the segment length to 11% of the total beam length which is the case shown in the figure. Compared to the Grade 50 steel, the greater ratio of ultimate to yield stress for A36 steel means that the yielding will spread a greater distance into the beam. For the elastofiber element with a single fiber segment at each end, this is better modeled with longer segments. Another effect is that the maximum strains at the ends of the beam will be reduced for the same end rotations. This is consistent with the absence of fiber rupture in the results with A36 steel.

For a beam in double curvature, the moment gradient is constant along the length of the element and scales inversely with the length. Since the length of the fiber segment in the elastofiber element is specified as a fraction of its length, it should be fairly invariant to moment gradient. The effect of axial load on the calibration of fiber segment length is less obvious. Axial load changes the stress distribution in the fibers across the cross-section (increase the stress in half the fibers and reduces the stress in the other half), but on the average it does not increase or decrease the distance into the beam up to which yielding spreads, hence the length of the fiber segment cannot

be reasonably scaled up or down based on the axial load in the absence of experimental data.

EXAMPLES

A three-dimensional nonlinear building analysis program, FRAME3D (Krishnan 2003), based on the analysis procedure described in the companion paper has been developed. It incorporates the plastic hinge and elastofiber beam elements, the panel zone element and the diaphragm element. The capabilities of FRAME3D are demonstrated through four examples: (1) elastic large deflection of a long cantilever beam, (2) cyclic loading of a cantilever beam, (3) comparison of the pushover analysis of a structural model of a 20-story building consisting of 3-dimensional elastofiber and panel zone elements against one consisting of 2-dimensional, 8-segment fiber elements (Hall and Challa 1995) and 2-dimensional panel zone elements, and (4) strong ground motion analysis of a 2-story unsymmetric steel moment-frame building.

Large Deflection of an Elastic Cantilever Beam

The problem of the large deflection of an elastic cantilever beam with a vertical point load at the free end (Figure 7) has been analyzed by (Mattiasson 1980) using elliptic integrals. This problem has been commonly used in the examination of finite element procedures for geometrically nonlinear beam analysis. Shown in Figure 8 is the comparison of the elliptic integral solution and that using elastofiber elements. The beam is discretized into 10 elastofiber elements. The load P is increased and the horizontal (u) and vertical (w) deflections of the free end are computed. These displacements are normalized by the length L and plotted against the load P normalized by $\frac{EI}{L^2}$. The close match demonstrates the geometric updating capabilities of the elastofiber element solution. The small error may be attributed to the omission of shear and axial deformations in the elliptic integral solution.

Cyclic Loading of a Cantilever Beam

The second example consists of a $W21 \times 57$ cantilever beam (Figure 9) of length 2.44m (96in) subjected to a specified cyclic vertical displacement, w, at the free end as also shown in the figure. Two cases are considered - the first without any axial load for which experimental results are available (Engelhardt and Husain 1992; Engelhardt and Husain 1993; Kim and Engelhardt 2000) and the second with a constant axial compressive load of $0.3P_y = 909.5\ kN\ (204.4\ Kips)$. Measured values of σ_y of 281.4 MPa (40.8 ksi) and σ_u of 415.2 MPa (60.2 ksi) were employed in the analysis, along with assumed values of $E = 2 \times 10^5\ MPa\ (29000\ ksi)$, $\epsilon_{sh} = 0.012$, $\epsilon_u = 0.160$, $\epsilon_r = 0.308$, $E_{sh} = 4000\ MPa\ (580\ ksi)$, and $G = 8 \times 10^4\ MPa\ (11600\ ksi)$. The experimental setup is given in Figure 9). Analysis was carried out using three elastofiber elements with fiber segment length of $11\%L$ for the two elements modeling the column and $22\%L$ for the element modeling the cantilever beam as well as using three 2-dimensional, 8-segment fiber elements (Hall and Challa 1995) for comparison with the experimental data. Shown in Figure 10 are results for the first case: the history of the beam shear force Q resulting from the specified displacement, and a plot of Q versus the free-end vertical displacement w. Results for the two beam elements match quite well, and they also agree with the experimental data up to the time that local flange buckling decreases the moment capacity of the test specimen (buckling occurs at load step 128). Even before this time, the response is well into the nonlinear range.

In Figure 11, results using elastofiber elements are compared to those using 2-dimensional 8-segment elements for the case with axial load present. Included in the figure are plots of the history of Q, Q versus w, and Q versus the axial displacement u. The constant axial load causes a greater moment to be reached and an axial displacement which continues to increase as the beam cycles up and down. Agreement between the two elements for the Q history and Q versus w curves is very good, comparable to the case without axial load. Axial displacements predicted using the elastofiber elements are within 20% of those using the more accurate 8-segment fiber elements.

Pushover Analysis of a 20-Story Building

In 1997, a study comparing buildings designed according to the 1994 Uniform Building Code (ICBO 1994) and the Japanese code provisions at that time was done by (Hall 1997). One of the structures examined was a 20-story steel moment-frame building designed per the 1994 UBC. A modified version of this building is subjected to a pushover analysis here to compare results using the 2-dimensional, 8-segment fiber element and the 2-dimensional panel zone element, as was done in (Hall 1997), with results from the new program FRAME3D. The modifications include omission of the following items: residual stresses, the contribution to strength and stiffness of the beams from the slab, web doubler plates, and the basement story. Both analyses include geometric stiffness and nodal updating.

Plan, section and perspective views of the building are shown in Figures 12, 13, and 14; included in Figure 13 are the beam and column designations. Columns are fixed at ground level. The following material properties are chosen for beam elements: $\sigma_y = 289.7\ MPa\ (42\ ksi)$, $\sigma_u = 344.9\ MPa\ (50\ ksi)$, $E = 2 \times 10^5\ MPa\ (29000\ ksi)$, $\epsilon_{sh} = 0.012$, $\epsilon_u = 0.160$, $\epsilon_r = 0.308$, $E_{sh} = 4000\ MPa\ (580\ ksi)$, and $G = 8 \times 10^4\ MPa\ (11600\ ksi)$. For the panel zone elements, the shear yield stress $\tau_y = 165.5\ MPa\ (24\ ksi)$ and the same shear modulus G is used.

The building is subjected to gravity loads and then pushover in the short direction (X direction). Gravity loads are based on roof dead load of 3840 $\frac{N}{m^2}$ (80 psf), floor dead load of 4550 $\frac{N}{m^2}$ (95 psf), cladding dead load of 1180 $\frac{N}{m^2}$ (24.6 psf), and reduced floor and roof live loads of 720 $\frac{N}{m^2}$ (15 psf). The pushover is run as an undamped dynamic analysis in which the base of the building is subjected to a ramped acceleration in the X direction linearly increasing at the constant rate of $0.3g$ per minute. Masses at the translational degrees of freedom are based on the gravity loads but are rearranged to give a distribution proportional to the 1994 UBC (ICBO 1994) static seismic design loads. The 2-dimensional analysis considers the moment frames on grid lines A and E as planar frames and the 12 columns on grid lines B, C, and D, as individual columns. These pieces are hooked together at each floor level by springs to simulate rigid diaphragm action. The

FRAME3D model is a full 3-dimensional representation of the building except that the exterior moment-frame beams on gridlines 1 and 4 are omitted. The floors and roof are modeled with stiff diaphragm elements, and no interior beams are included. Figure 14 shows the elastofiber elements (dark lines) and diaphragm elements (gray rectangles) of the FRAME3D model. The two models should be comparable, and any differences can be attributed mainly to the use of the 8-segment fiber element in the 2-dimensional analysis and the elastofiber element in the FRAME3D analysis.

Results are shown in Figure 15 in the form of time histories of the base shear force generated at the base of the columns and time histories of the roof displacement, both in the X direction. The agreement is very good, and this provides a successful test of many, but not all, features of FRAME3D and also of the effectiveness of the elastofiber element. As is evident from the figure, the analysis has been carried well into the range where the base shear reduces, which is due to a combination of strain softening and $P - \Delta$ effects.

Strong Ground Motion Analysis of a 2-Story Asymmetric Moment Frame Building

The last example is a 2-story steel moment frame building with two bays in each direction. The model consists of 27 nodes, 30 beam elements to model beams and columns, 8 diaphragm elements for the second floor and roof, and 14 panel zone elements. The plan of the building with column orientations and location of moment frame connections appears in Figure 16 and a perspective view is shown in Figure 17. To create an unsymmetric structure, moment frames are present on only three out of four faces of the building. The X-direction moment frame on the $+Y$ face has been omitted. Figure 17 indicates the beam elements (dark lines) and diaphragm elements (gray rectangles) of the FRAME3D model. The beam elements are elastofiber elements except for the two non-moment-frame columns on grid line 2 which are plastic hinge elements. No beams are included along grid lines 2, B and C.

All columns are W14x68 AISC steel sections and all moment frame beams are W16x40 AISC steel sections. For the beam elements, A572-Grade 50 steel with σ_y of 345 MPa (50 ksi)

is used. Other parameters for the elastofiber elements are $\sigma_u = 448\ MPa\ (65\ ksi)$, $E = 2 \times 10^5\ MPa\ (29000\ ksi)$, $\epsilon_{sh} = 0.012$, $\epsilon_u = 0.160$, $\epsilon_r = 0.308$, $E_{sh} = 4000\ MPa\ (580\ ksi)$, and $G = 8 \times 10^4\ MPa\ (11600\ ksi)$. In addition, $k_1 = k_2 = 0.15\frac{EI}{L}$ for the plastic hinge elements. For the panel zone elements, $\tau_y = 199\ MPa\ (28.9\ ksi)$ and the same G is used. The diaphragm elements have a thickness of 114 mm (4.5 in), E of 24830 MPa, and Poisson's ratio ν of 0.3.

A uniform dead load of 4790 $\frac{N}{m^2}$ (100 psf) is assumed for the second floor and a uniform dead load of 3832 $\frac{N}{m^2}$ (80 psf) is assumed for the roof. A reduced live load of 575 $\frac{N}{m^2}$ (12 psf) is assumed to be present on the second floor and roof at the time of the earthquake, which is included both as a gravity load and in the structural mass. The center of mass of both the second floor and the roof lie at the center of the floor plan (grid location B-2). However, due to the position of the moment frame in the X direction, the center of resistance lies very close to grid line A. The mass and stiffness proportional damping coefficients α_0 and α_1 are computed to give 2% damping at periods of 0.05 and 0.30 seconds. The building is subjected to ground shaking from the 74° Azimuth (approximately EW) horizontal component of the Tabas strong-motion record from the 1978 Iran earthquake (Figure 18) which is applied in the X direction. Although the program has the capacity to handle all three components of ground motion, in this example, a single component is employed to make the twisting component of the response more clear. Twisting occurs for ground motion in the X direction because of the eccentricity between the centers of mass and stiffness.

Results of the FRAME3D analysis are shown in Figures 19, 20, and 21. Time histories of roof displacement are presented in Figure 19 for diagonally opposite grid locations A-1 and C-3. Twisting of the building amplifies the X-direction motion at C-3 compared to that at A-1 and also causes Y-direction motions which are out-of-plane at these two locations. Figure 20 demonstrates the bi-axial bending at the base of the column at grid location C-1 with a path plot of $M_{Y'}$, $M_{Z'}$ pairs during the time history. Also shown on this plot are lines corresponding to the major axis and minor axis plastic moment capacities of the section, $\pm M^0_{pY'}$ and $\pm M^0_{pZ'}$, as well as the actual moment capacity curve computed considering interaction among the major axis and minor axis moments and the static axial force $\frac{P}{P_y} = 0.032$. All of these capacities are based on σ_y and, so,

do not consider strain hardening. Finally, peak values of plastic shear strain in the panel zones (only the ① panels yield, see Figure 1 in the companion paper) and peak values of plastic rotations at the ends of the columns (major and minor axis bending for columns and major axis bending for beams) are presented in Figure 21. Some significant yielding occurs in the moment frame on grid line A, which provides lateral resistance in the direction of the ground motion. This is accompanied by significant minor axis plastic hinging at the bases of columns on grid lines B and C, which is increased by the twisting. At the base of column C-1, whose moment path appears in Figure 20, the plastic rotations reach 0.7 and 2.4 percent radians about the major and minor axes, respectively. The twisting also induces loading of the perpendicular moment frames on lines 1 and 3 enough to cause moderate yielding at a few locations. The total execution time for 25 seconds of ground motion with a time step of 0.005 seconds is 22.99 minutes (on a 3GHz linux box) of which 20.83 minutes are spent in local member iterations. Since a major portion of the analysis time is spent in local member structural analysis, using the elastofiber element as opposed to the fully discretized fiber element represents significant savings in computer time (for an 8-segment fiber element, the local structural analysis involves solving a 54 equation system as opposed to the 24 equation system for the elastofiber element). For larger buildings with more degrees of freedom, the time spent in global iterations would be relatively greater, but since the number of beam elements would also go up (leading to greater time spent in member iterations), the savings would still be substantial. This example demonstrates many of the 3-dimensional capabilities of FRAME3D.

CONCLUSIONS

The elastofiber beam element developed here is intended for three-dimensional modeling of beams and columns in steel structures. The element is divided into three segments - two end nonlinear segments and an interior elastic segment. The division of the end segment cross-sections into fibers, with a nonlinear hysteretic stress-strain law for axial stress and strain associated with each

fiber, allows for the nonlinear coupling between bending about the major and minor axes of the cross-section and axial deformation. A calibration study performed on a beam subjected to rotation histories at its two ends causing cyclic double curvature in the beam indicate close agreement between the elastofiber element and an 8-segment fiber element, even under plastic rotations up to 10% of a radian. An end segment length of 3% of the span is suitable for materials with low ultimate stress to yield stress ratios (less than 1.4) such as A572-Grade 50 steel, and an end segment length of 11% of the span is suitable for materials with high ultimate stress to yield stress ratios (greater than 1.4) such as A36 steel. The four examples presented here illustrate the ability of the analysis procedure, incorporating plastic hinge and elastofiber beam elements, panel zone elements and diaphragm elements, in modeling inelastic static and dynamic structural behavior, including large displacement and three-dimensional response.

References

Challa, V. R. M. (1992). Nonlinear seismic behavior of steel planar moment-resisting frames. Technical Report EERL 92-01, Earthquake Engineering Research Laboratory, California Institute of Technology, Pasadena, California.

Engelhardt, M. D. and A. S. Husain (1992). Cyclic tests on large-scale steel moment connections. Technical Report Res. Rep. PMFSEL 92-2, Dept. of Civil Engineering, University of Texas, Austin, Texas.

Engelhardt, M. D. and A. S. Husain (1993). Cyclic-loading performance of welded flange-bolted web connections. *Journal of Structural Engineering, ASCE 119*(12), 3537–3550.

Hall, J. F. (1995). Parameter study of the response of moment-resisting steel frame buildings to near-source ground motions. Technical Report EERL 95-08, Earthquake Engineering Research Laboratory, California Institute of Technology, Pasadena, California.

Hall, J. F. (1997). Seismic response of steel frame buildings to near-source ground motions. Technical Report EERL 97-05, Earthquake Engineering Research Laboratory, California Institute of Technology, Pasadena, California.

Hall, J. F. and V. R. M. Challa (1995). Beam-column modeling. *Journal of Engineering Mechanics 121*(12), 1284–1291.

ICBO (1994). *1994 Uniform Building Code*. Volume 2. International Conference of Building Officials, Whittier, California.

Kaba, S. and S. A. Mahin (1984). Refined modeling of reinforced concrete columns for seismic analysis. Technical Report UCB/EERC-84-03, Earthquake Engineering Research Center, University of California, Berkeley, California.

Kim, K. D. and M. D. Engelhardt (2000). Beam-column element for nonlinear seismic analysis of steel frames. *Journal of Structural Engineering, ASCE 126*(8), 916–925.

Krishnan, S. (2003). FRAME3D - a program for three-dimensional nonlinear time-history anal-

ysis of steel buildings: User guide. Technical Report EERL 2003-03, Earthquake Engineering Research Laboratory, California Institute of Technology, Pasadena, California.

Mark, K. M. S. (1976). Nonlinear dynamic response of reinforced concrete frames. Technical Report R76-38, Department of Civil Engineering, Massachusetts Institute of Technology, Cambridge, Massachusetts.

Mattiasson, K. (1980). Numerical results from large deflection beam and frame problems analyzed by means of elliptic integrals. *International Journal for Numerical Methods in Engineering 17*((1)), 145–153.

List of Figure Captions

Figure 1. Layout of the 3-Segment Elastofiber Element (Fiber Arrangement is Shown for an I Section and a Box Section).

Figure 2. Local DOF of a Segment of the Elastofiber Beam Element Showing Nodal Translations and Rotations and Nodal Forces and Moments.

Figure 3. Axial Stress-Strain Model for a Fiber in an Elastofiber Element.

Figure 4. Simply Supported Beam and Applied Rotation History θ Used for Calibration Studies.

Figure 5. Calibration Study: Comparison of Elastofiber Element with 8-Segment Fiber Element ($\sigma_y = 345\ MPa;\ \sigma_u = 448\ MPa$).

Figure 6. Calibration Study: Comparison of Elastofiber Element with 8-Segment Fiber Element ($\sigma_y = 248\ MPa;\ \sigma_u = 400\ MPa$).

Figure 7. Cantilever Beam for Large Deflection Example.

Figure 8. Large Deflection of a Cantilever Beam: Comparison of Response Using Elastofiber Elements with Analytical Solution.

Figure 9. Cantilever Beam and Applied Displacement History, w, Used for Cyclic Loading Example.

Figure 10. Cycled Cantilever Beam: Comparison of Experiment, Elastofiber Element and 8-Segment Fiber Element.

Figure 11. Cycled Cantilever Beam with Axial Load: Comparison of Elastofiber and 8-Segment Fiber Element.

Figure 12. Typical Floor Plan of 20-Story Building.

Figure 13. Sections A (Left) and B (Right) of 20-Story Building Showing AISC Member Designations.

Figure 14. Perspective View of 20-Story Building as Modeled by FRAME3D.

Figure 15. Pushover of 20-Story Building in the X-Direction: Comparison of 3-Dimensional Elastofiber Element and 2-Dimensional 8-Segment Fiber Element Models.

Figure 16. Floor Plan of 2-Story Unsymmetric Building.

Figure 17. Perspective View of 2-Story, Unsymmetric Building as Modeled by FRAME3D.

Figure 18. 74° Azimuth (approximately EW) Horizontal Component of 1978 Iran Earthquake Tabas Acceleration Record.

Figure 19. Two-Story Unsymmetric Building: Displacement Time-Histories of Grid Corner Locations A-1 and C-3 at Roof Level.

Figure 20. Two-Story Unsymmetric Building: $M_{Y'} - M_{Z'}$ Path at the Base of Column at Grid Intersection C-1.

Figure 21. Two-Story Unsymmetric Building: Peak Plastic Shear Strains in Panel Zones (Boxes) and Plastic Rotations at the Ends of Beams and Columns (Ovals), in % of a Radian

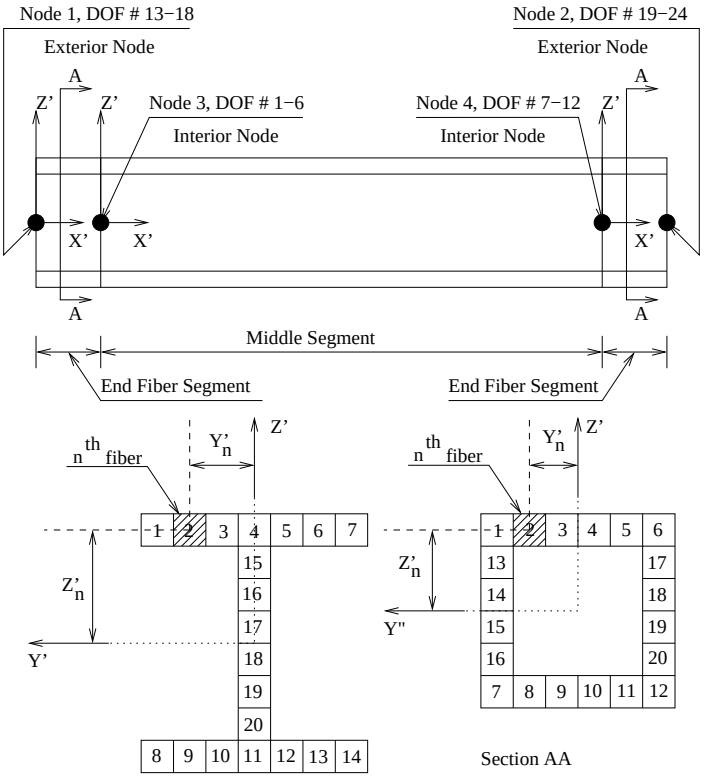

Figure 1: Layout of the 3-Segment Elastofiber Element (Fiber Arrangement is Shown for an I Section and a Box Section)

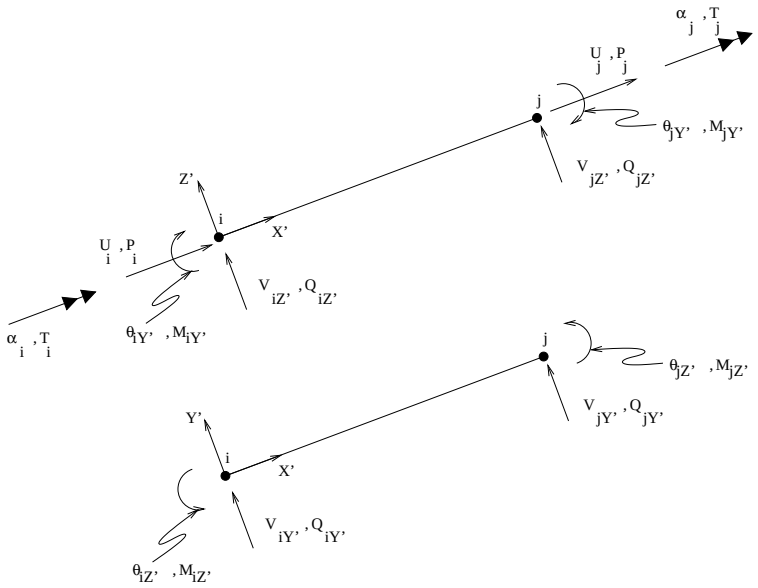

Figure 2: Local DOF of a Segment of the Elastofiber Beam Element Showing Nodal Translations and Rotations and Nodal Forces and Moments

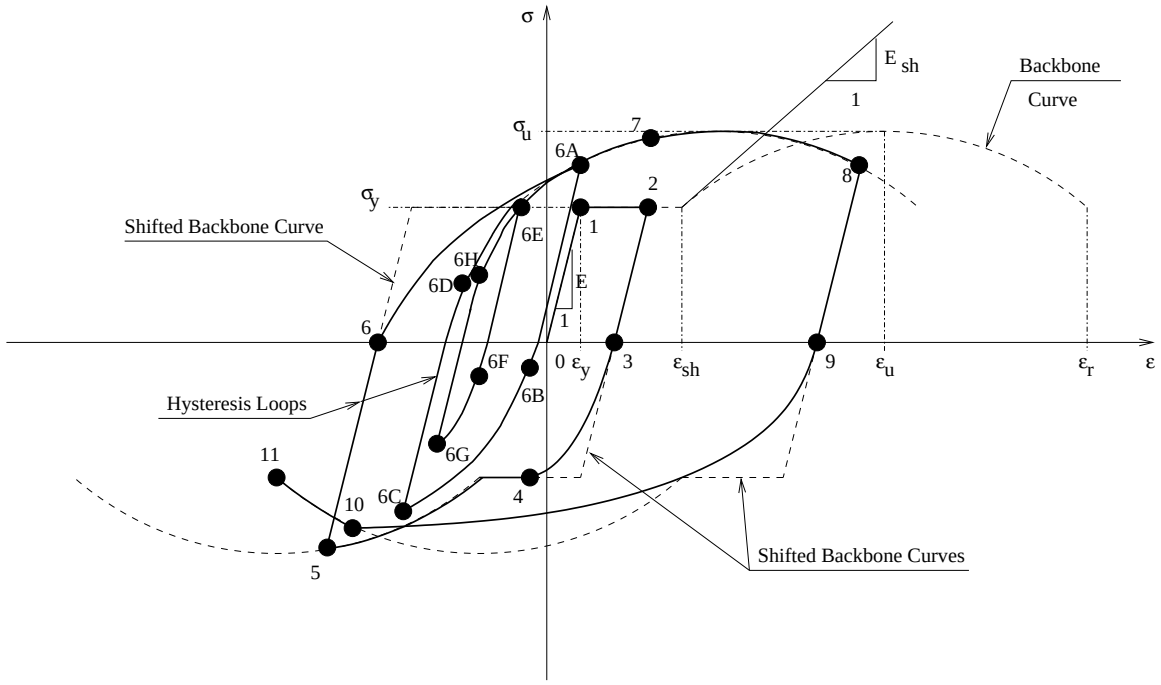

Figure 3: Axial Stress-Strain Model for a Fiber in an Elastofiber Element

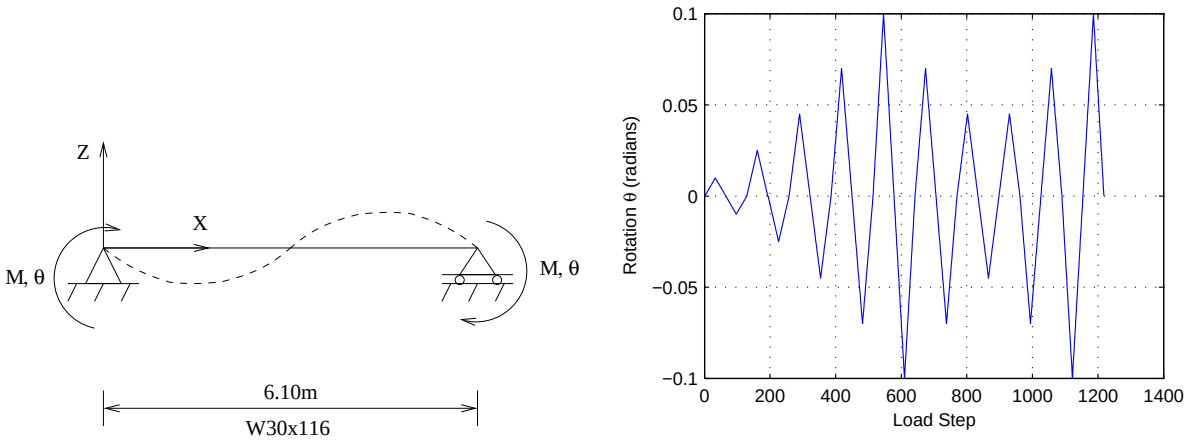

Figure 4: Simply Supported Beam and Applied Rotation History θ Used for Calibration Studies

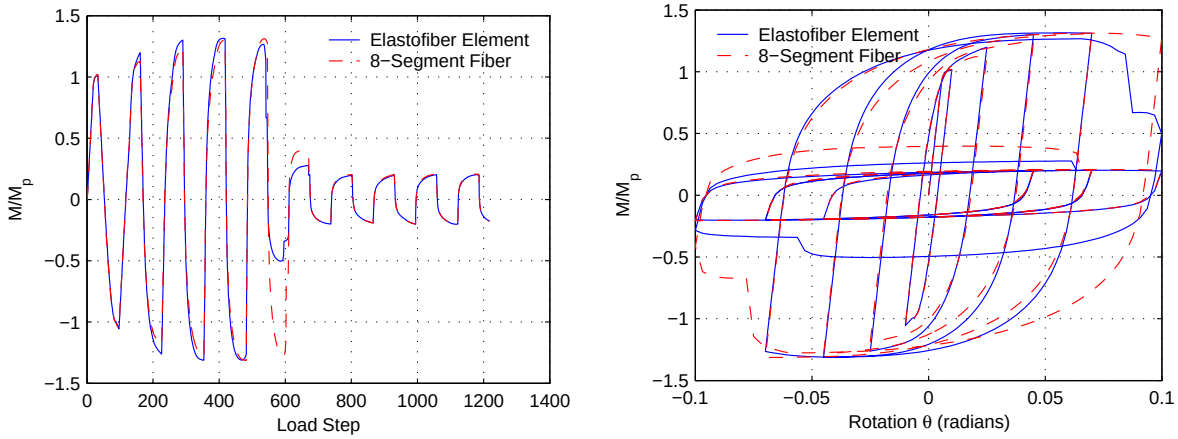

Figure 5: Calibration Study: Comparison of Elastofiber Element with 8-Segment Fiber Element ($\sigma_y = 345\ MPa;\ \sigma_u = 448\ MPa$)

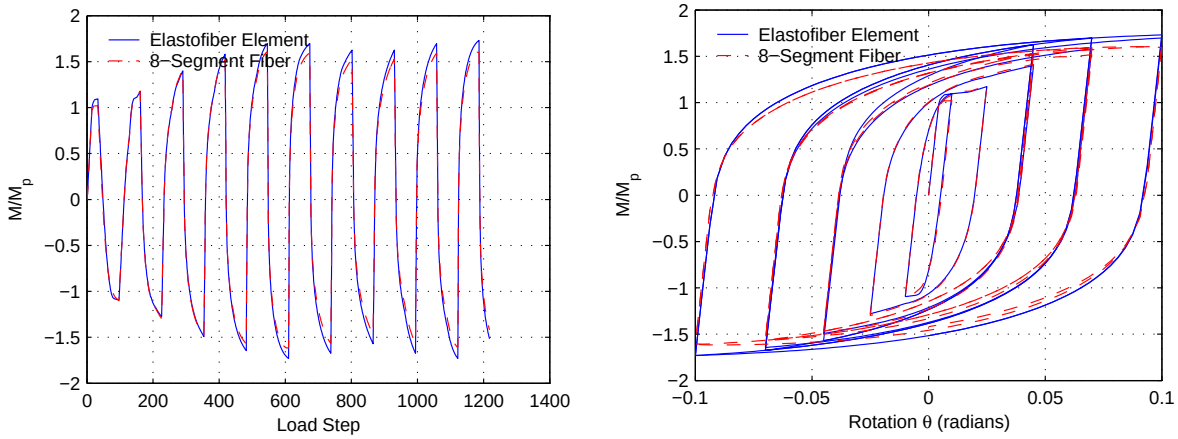

Figure 6: Calibration Study: Comparison of Elastofiber Element with 8-Segment Fiber Element ($\sigma_y = 248\ MPa;\ \sigma_u = 400\ MPa$)

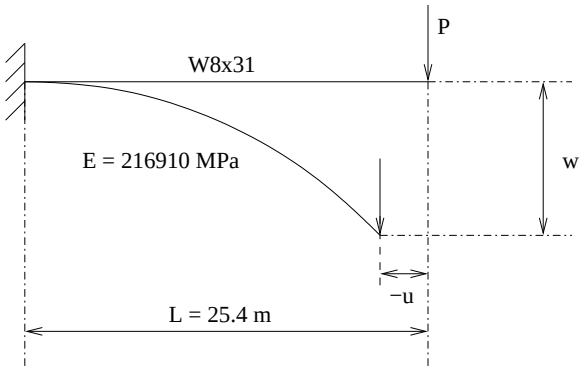

Figure 7: Cantilever Beam for Large Deflection Example

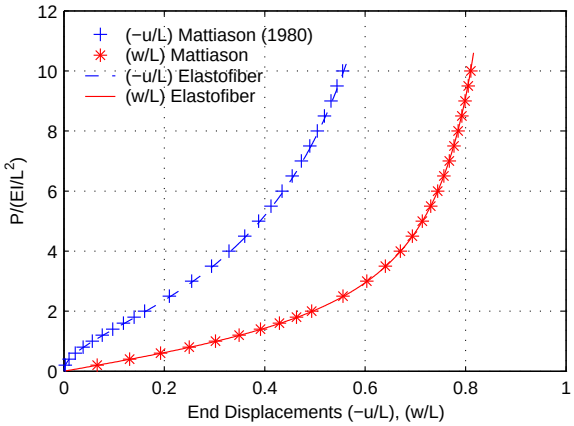

Figure 8: Large Deflection of a Cantilever Beam: Comparison of Response Using Elastofiber Elements with Analytical Solution

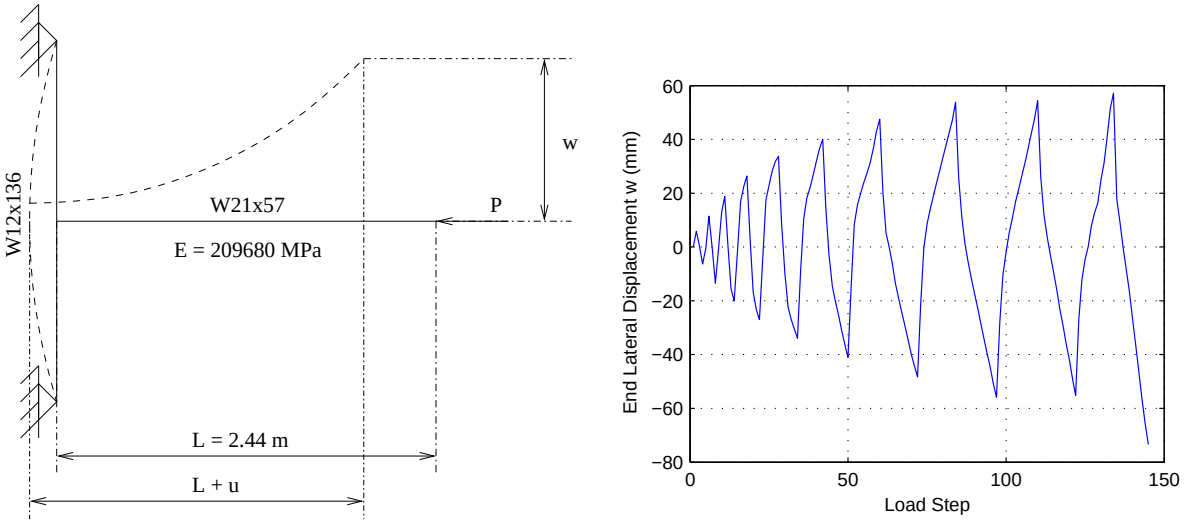

Figure 9: Cantilever Beam and Applied Displacement History, w, Used for Cyclic Loading Example

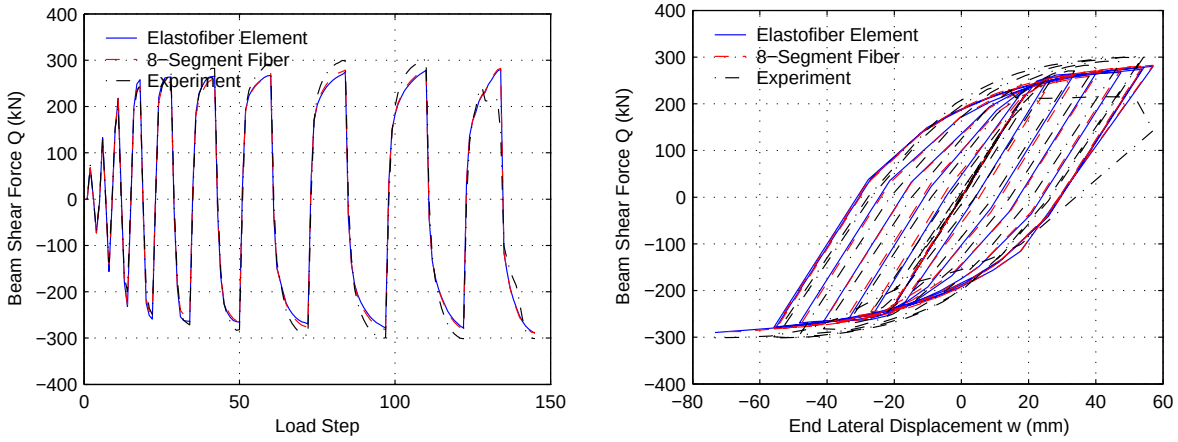

Figure 10: Cycled Cantilever Beam: Comparison of Experiment, Elastofiber Element and 8-Segment Fiber Element

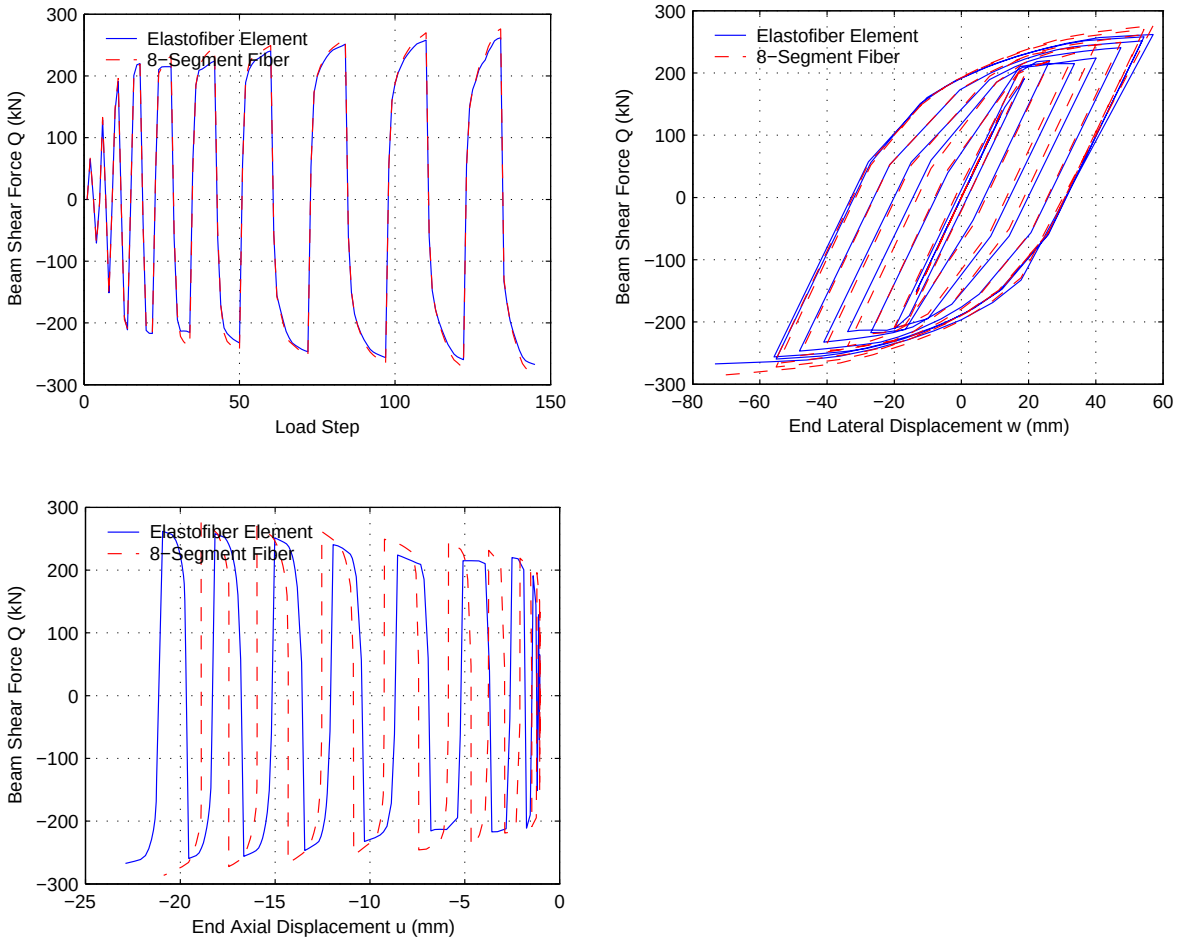

Figure 11: Cycled Cantilever Beam with Axial Load: Comparison of Elastofiber and 8-Segment Fiber Element

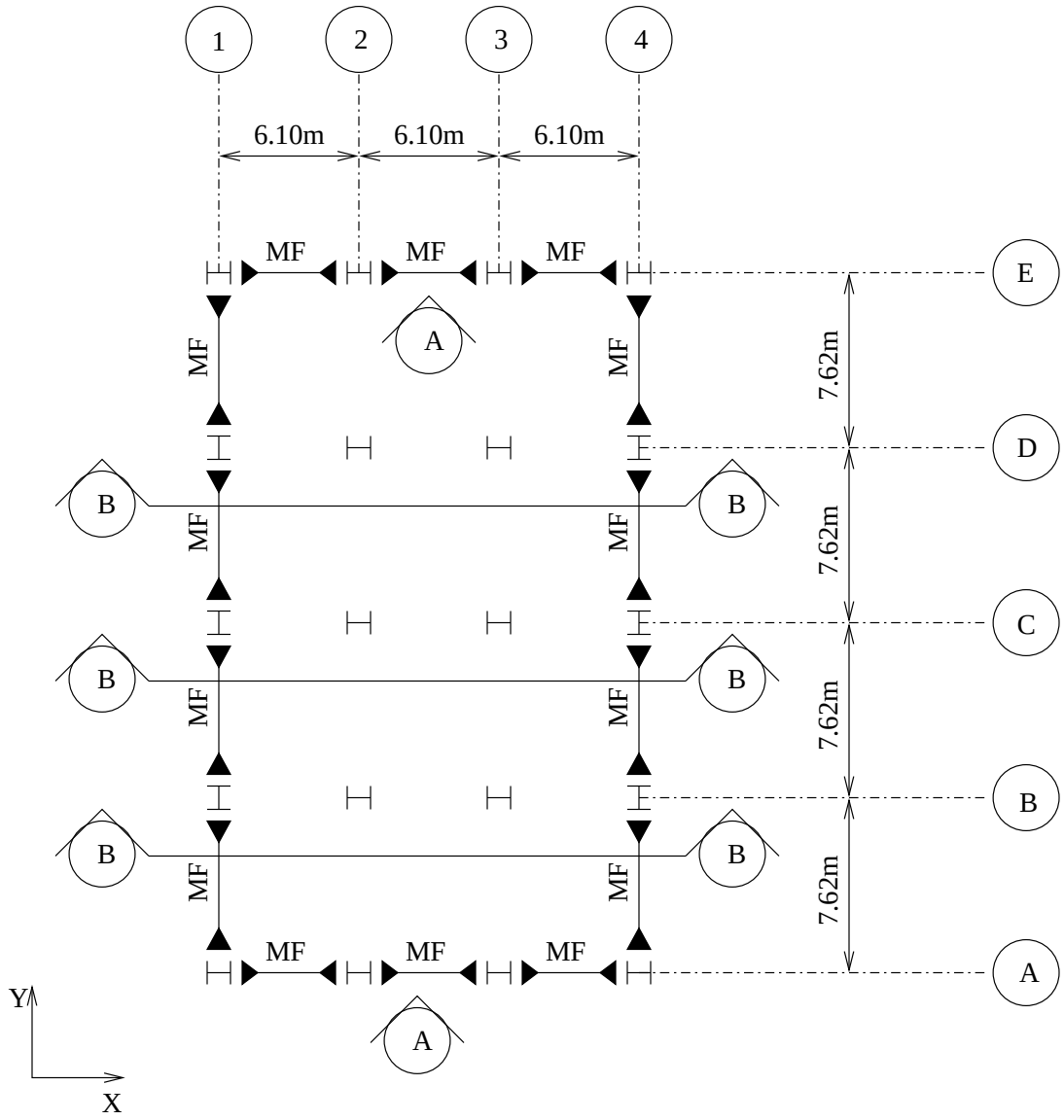

Figure 12: Typical Floor Plan of 20-Story Building

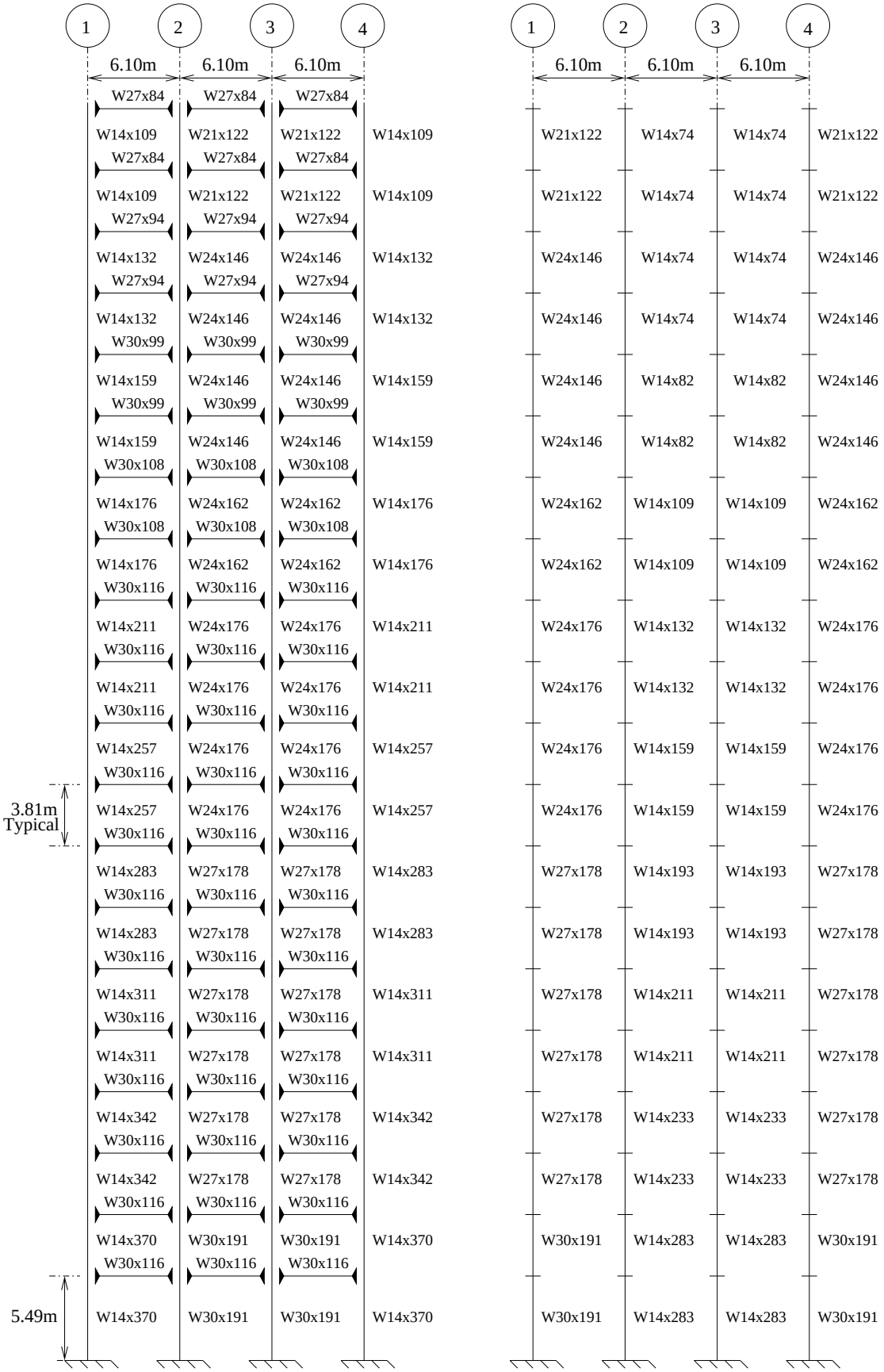

Figure 13: Sections A (Left) and B (Right) of 20-Story Building Showing AISC Member Designations

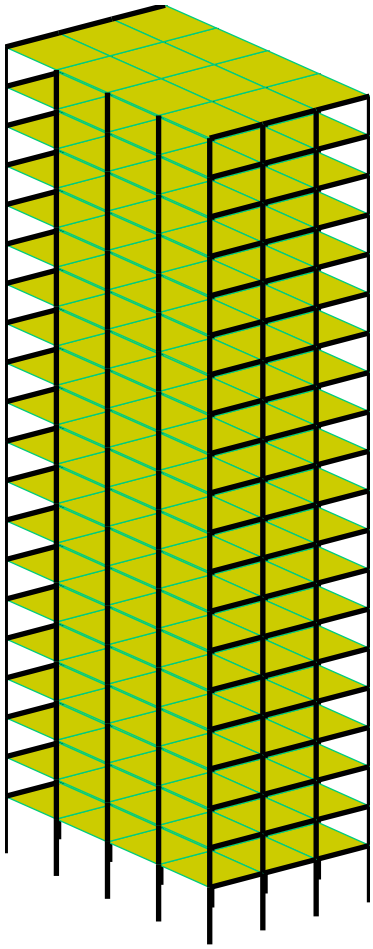

Figure 14: Perspective View of 20-Story Building as Modeled by FRAME3D

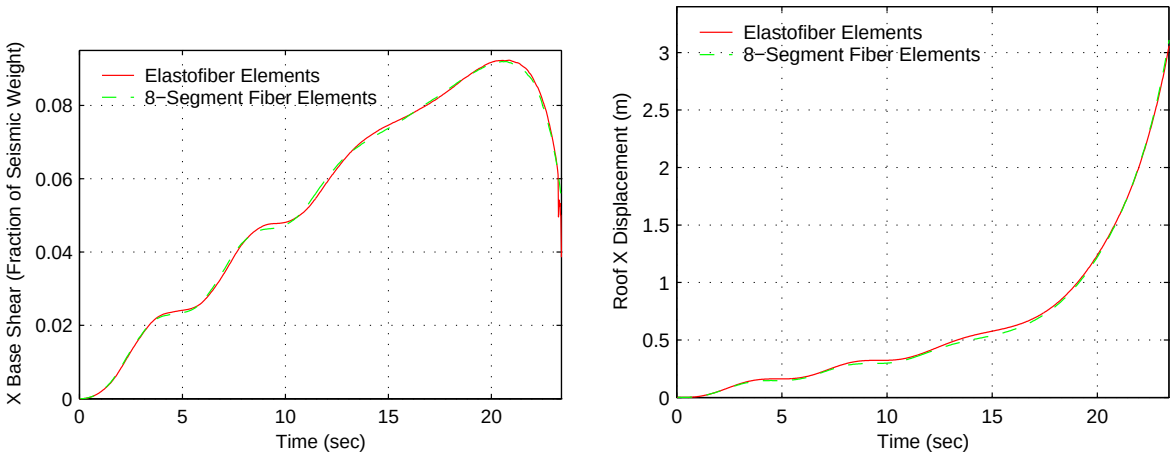

Figure 15: Pushover of 20-Story Building in the X-Direction: Comparison of 3-Dimensional Elastofiber Element and 2-Dimensional 8-Segment Fiber Element Models.

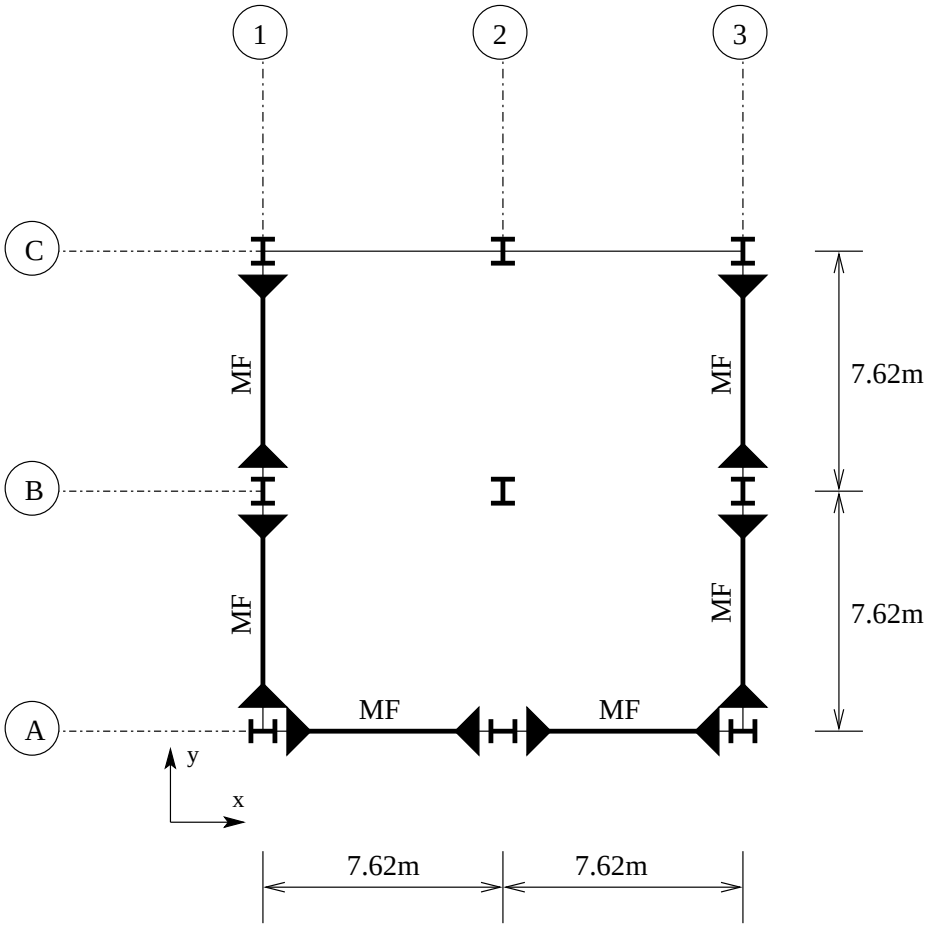

Figure 16: Floor Plan of 2-Story Unsymmetric Building

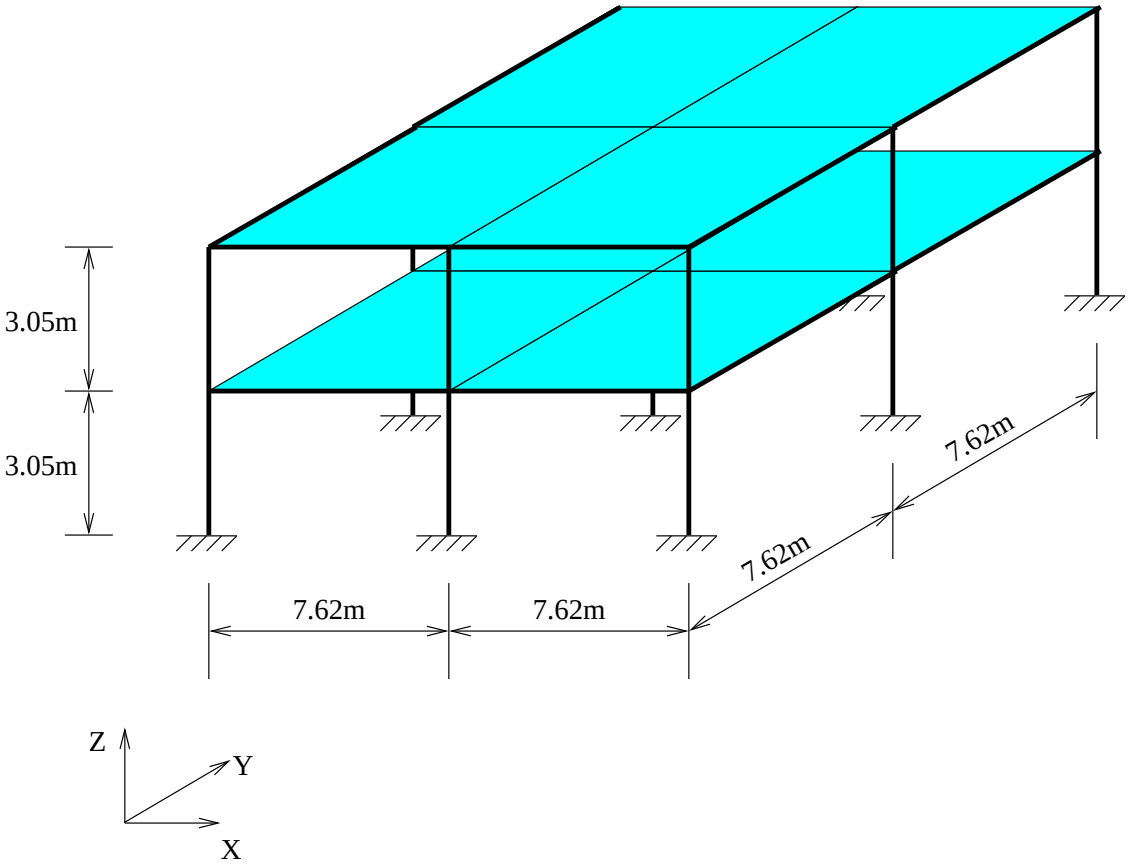

Figure 17: Perspective View of 2-Story, Unsymmetric Building as Modeled by FRAME3D

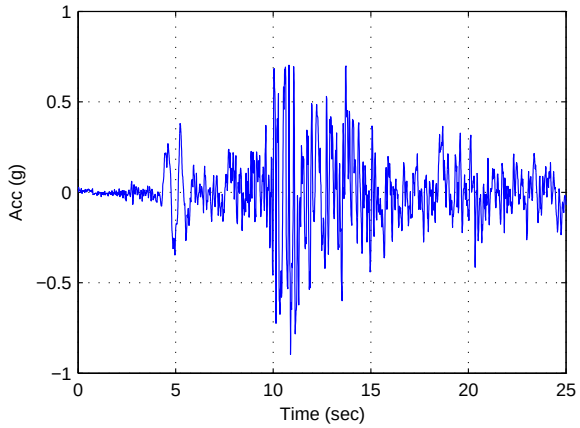

Figure 18: 74° Azimuth (approximately EW) Horizontal Component of 1978 Iran Earthquake Tabas Acceleration Record

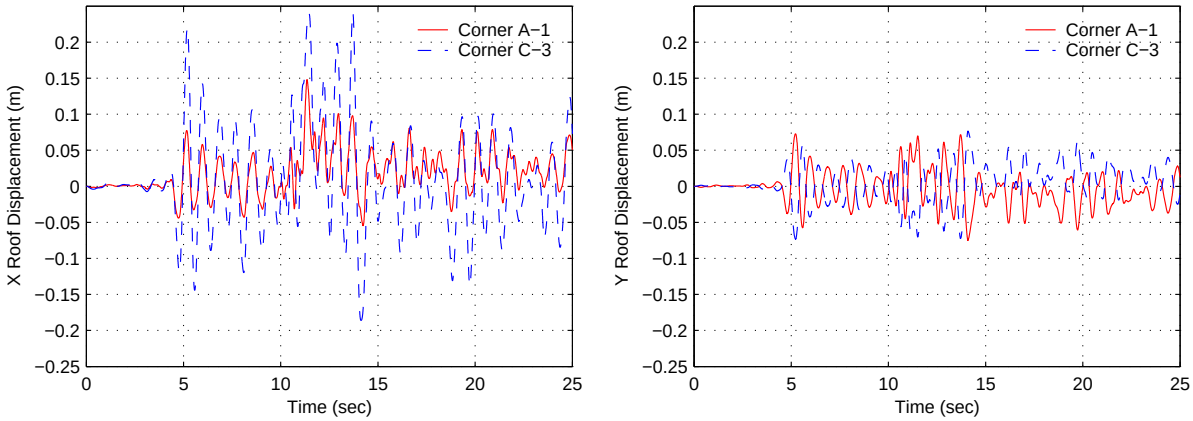

Figure 19: Two-Story Unsymmetric Building: Displacement Time-Histories of Grid Corner Locations A-1 and C-3 at Roof Level

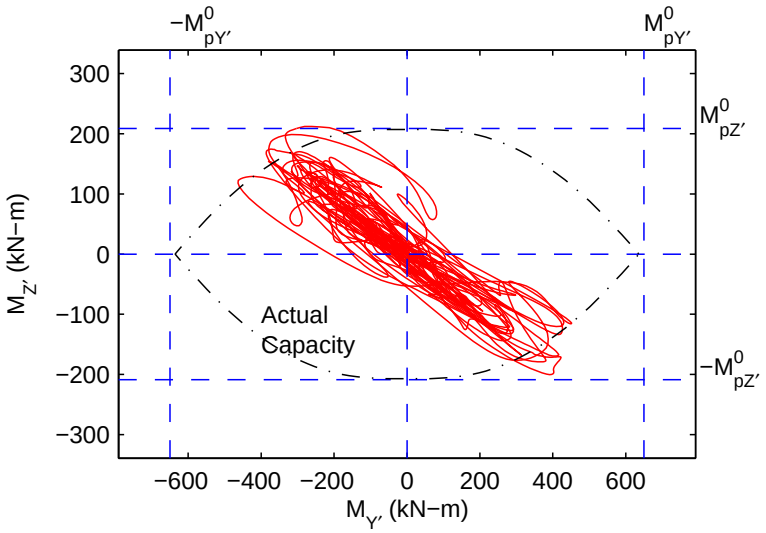

Figure 20: Two-Story Unsymmetric Building: $M_{Y'} - M_{Z'}$ Path at the Base of Column at Grid Intersection C-1

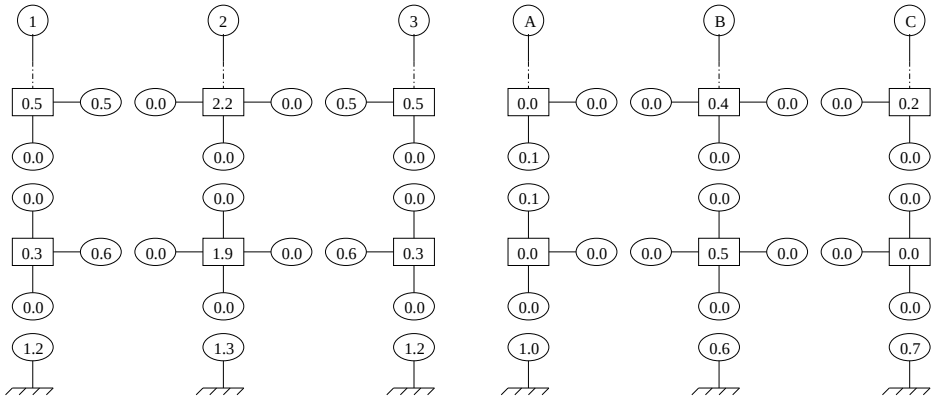

(a) Gridline A (b) Gridline 1

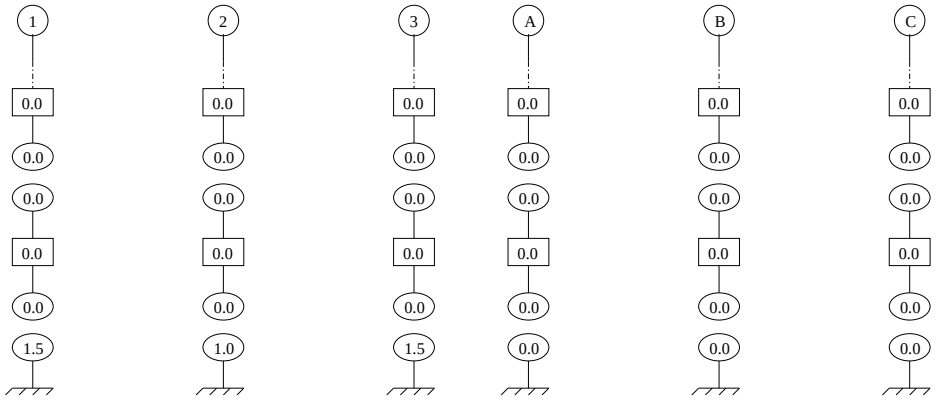

(c) Gridline B (d) Gridline 2

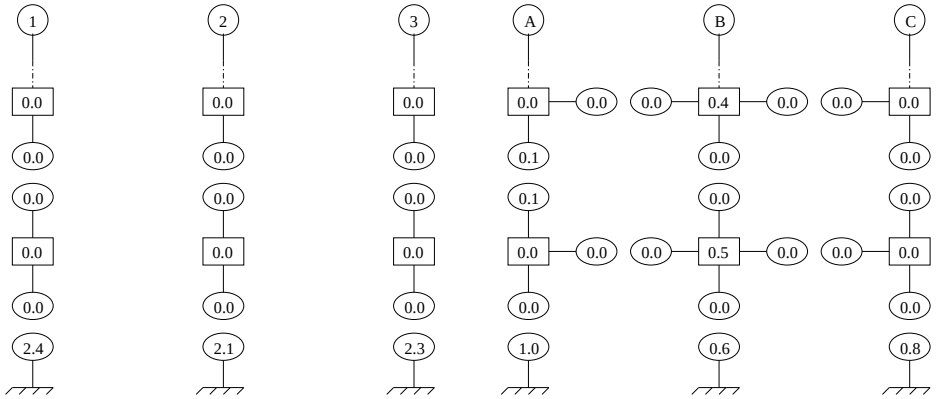

(e) Gridline C (f) Gridline 3

Figure 21: Two-Story Unsymmetric Building: Peak Plastic Shear Strains in Panel Zones (Boxes) and Plastic Rotations at the Ends of Beams and Columns (Ovals), in % of a Radian